Phase-field simulation of solid state sintering

Johannes Hötzer[a,b,1,*], Marco Seiz[a,1], Michael Kellner[a,b,1], Wolfgang Rheinheimer[c], Britta Nestler[a,b]

[a] *Institute for Applied Materials (IAM), Karlsruhe Institute of Technology (KIT), Straße am Forum 7, 76131 Karlsruhe, Germany*
[b] *Institute of Digital Materials (IDM), Karlsruhe University of Applied Sciences, Moltkestrasse 30, D 76133 Karlsruhe, Germany*
[c] *School of Materials Engineering, Purdue University, 701 West Stadium Avenue, West Lafayette, IN 47907-2045, USA*

Abstract

In order to produce tailored ceramics with defined properties a deep knowledge about the sintering process and especially the underlying microstructure evolution is required. Due to the complex interplay of the material and process parameters as well as complex geometries, it is challenging to predict the microstructure evolution during sintering with analytical models. Especially the phase-field method has been established as a versatile tool to investigate microstructure evolution under the influence of various physical phenomena. To describe the microstructural evolution during solid state sintering, a phase-field model based on the grand potential approach considering volume, surface and grain boundary diffusion is presented. To efficiently investigate realistic green bodies with multiple thousand particles in three dimensions, the model is implemented in a highly optimized manner in the massive parallel phase-field solver framework Pace3D. By comparing the neck growth rates in a two particle system for the different diffusion mechanisms a good agreement to analytic solutions is found. Based on a three dimensional green body of 24 897 grains the densification depending on the dominant diffusion mechanisms is investigated and compared with the analytic Coble model. Finally, the appearance of isolated pores in the microstructure is observed.

Keywords: Phase-field model, solid state sintering, diffusion mechanisms, Large-scale simulations, Microstructure analysis

1. Introduction

Ceramic materials have been manufactured by sintering process ('firing') for thousands of years, mostly in the field of pottery. Today, ceramics find

*Corresponding author. Tel.: +49 721 608-45315; Fax: +49 721 608-44364; email: johannes.hoetzer@kit.edu

[1] **The authors contributed equally.**

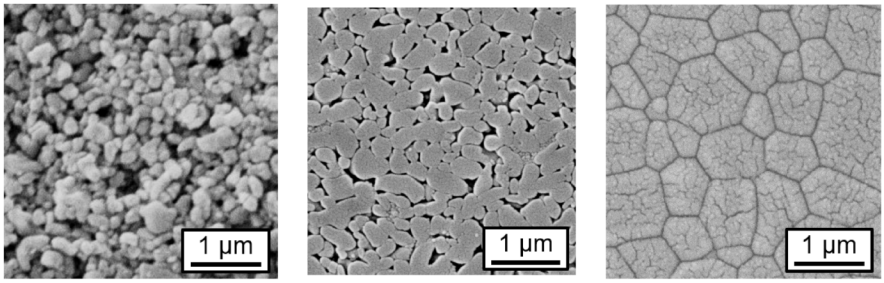

(a) Initial green body (b) After 30 minutes at 1240 °C (c) After 90 minutes at 1240 °C

Figure 1: Experimental micrographs of alumina from [5]

application in many electronic, security, health care, mobility and civil engineering products due to their unique functional and structural properties [1]. In most cases the manufacturing of ceramic parts includes a sintering process, so that sintering is a crucial process of materials science and engineering as the microstructure directly influences the properties of the materials. To develop new and improved materials with defined properties tailored microstructures are necessary, which require a deep understanding of the microstructure evolution [2]. Particularly an understanding of the underlying mechanisms of densification and grain growth and their interplay during sintering is of high interest for manufacturing and engineering of high performance ceramic parts.

Sintering is driven by a reduction of free surface area and results in a material redistribution in the contact area between powder particles. In general, the solid state sintering process can be divided into three stages: initial, intermediate and final stage sintering [3, 4]. Starting from a loose powder compact (Fig. 1(a)), in the initial stage the loose packed powder particles bind together and form sintering necks between each other. During the intermediate stage, most of the densification occurs which can be accompanied by grain growth (Fig. 1(b)). The final stage is characterized by the evolution of isolated pores in the microstructure and by grain growth in the almost dense solid (Fig. 1(c)). The microstructure evolution at these three stages is highly complex due to many physical processes interacting with each other. Especially the effects of particle sizes and different diffusion mechanisms — volume, grain boundary and surface diffusion — play a central role in the densification and coarsening process: without diffusion, either grain boundary or volume, in the contact area between two powder particles, densification cannot occur.

@All: Bildrechte?

In all stages the densification and coarsening process is affected by parameters like particle size distribution, initial density, interface energies and by mechanisms such as volume, grain boundary and surface diffusion. To describe the microstructure evolution in these stages various theoretical models have been developed. For the initial stage, simple two particle models are considered

to investigate the neck formation and densification[6–9]. The densification in the intermediate stage is analyzed by Coble [10, 11] assuming an interconnected pore channel network along the triple lines in which tetrakaidecahedronal grains of fixed size and shape are embedded. With this model the densification can be estimated, if parameters such as grain boundary energies and diffusion coefficients are known. Further grain growth and densification models for the final sintering stage are published in [10–18]. Summaries of different analytical approaches can be found in [3, 4, 19]. Although these models enable the investigation of the sintering process, they are of limited use for the understanding of the microstructure evolution since they assume an idealized geometry. A more general approach is the use of Herring's scaling laws [20], which relate the relative rate of sintering (e.g. neck growth or densification) to the size of the particles and the dominant diffusion mechanism.

Besides these analytical approaches the phase-field method has been established in the last decades as a powerful tool to study the microstructure evolution under the influences of various physical phenomena [2]. Early phase-field models considering a single pore in a polycrystal are derived in [21, 22]. Phase-field models to investigate two particle systems are developed in [23–31]. Simulations of green bodies for 2D domains are conducted in [23, 25, 28, 29, 32, 32] and for 3D domains in [33]. In contrast to the previously developed models a grand potential approach based on [34–36] is used to investigate the microstructure evolution for all three sintering stages. To describe the different diffusion mechanisms, an approach similar to [23, 25] is developed. The locally reduced order parameter approach of Kim et al. [37] is implemented in the Pace3D solver [38] to allow the modelling of large three-dimensional powder compacts consisting of multiple thousands particles. With this combined approach, this paper investigates the influence of different diffusion mechanisms on sintering and densification in realistic powder compacts.

2. Phase-field model for solid state sintering

In this section the model is defined and the evolution equations for the phase-fields and the chemical potentials are derived. Based on this, in the next section different optimizations to reduce the memory requirements and the computational effort in the case of a large number of order parameters in the Pace3D framework are introduced.

2.1. Derivation of the phase-field equation

For the model the domain $\Omega \subset \mathbb{R}^d$ with $d \in \{1, 2, 3\}$ is considered. The N different phases are labelled with the indices α, β and γ. To distinguish between the $N - 1$ grain phases and the surrounding vapor phase, the additional labels grain_1 to $\mathsf{grain}_{\mathsf{N}-1}$ and vap are introduced. The local thermodynamic state of these phases (e.g. phase fractions, orientation) at the position $\boldsymbol{x} \in \Omega$ and the time $t \in \mathbb{R}$ is described by the order-parameters $\phi_\alpha(\boldsymbol{x}, t)$ [36, 39] which is twice continuously differentiable in space. The order-parameters are

collected in the phase-field vector $\boldsymbol{\phi} : \Omega \rightarrow \Delta^{N-1}$ with the simplex $\Delta^{N-1} = \left\{\phi_1 \boldsymbol{e}_1 + \cdots + \phi_N \boldsymbol{e}_N \mid \phi_\alpha \geq 0 \wedge \sum_{\alpha=1}^{N} \phi_\alpha = 1\right\}$ and the basis vectors $\boldsymbol{e}_\alpha$ of a Cartesian coordinate system.

In order to model the total energy of the system, the grand potential functional Ψ of the form

$$\Psi(\boldsymbol{\phi}, \boldsymbol{\mu}, T) = \int_\Omega \Upsilon(\boldsymbol{\phi}, \nabla\boldsymbol{\phi}) + \psi(\boldsymbol{\phi}, \boldsymbol{\mu}, T) d\Omega \tag{1}$$

with the diffuse interface contribution $\Upsilon(\boldsymbol{\phi}, \nabla\boldsymbol{\phi})$ and the driving force $\psi(\boldsymbol{\phi}, \boldsymbol{\mu}, T)$ is used. The functional depends on the phase-field vector $\boldsymbol{\phi}$, the chemical potential vector $\boldsymbol{\mu}$ and the temperature T.

The diffuse interface contribution is written as

$$\Upsilon(\boldsymbol{\phi}, \nabla\boldsymbol{\phi}) = \varepsilon a(\boldsymbol{\phi}, \nabla\boldsymbol{\phi}) + \frac{1}{\varepsilon}\omega(\boldsymbol{\phi}) \tag{2}$$

with the gradient energy term $a(\boldsymbol{\phi}, \nabla\boldsymbol{\phi})$, the potential energy term $\omega(\boldsymbol{\phi})$ and the parameter ε, which is related to the interface thickness [40]. The gradient energy term is formulated as

$$a(\boldsymbol{\phi}, \nabla\boldsymbol{\phi}) = \sum_{\substack{\alpha,\beta=1 \\ (\alpha<\beta)}}^{N,N} \gamma_{\alpha\beta}[a_{\alpha\beta}(\vec{q}_{\alpha\beta})]|\vec{q}_{\alpha\beta}|^2 \,. \tag{3}$$

Here, $\gamma_{\alpha\beta}$ represents the interface energy density and $\vec{q}_{\alpha\beta} = \phi_\alpha \nabla\phi_\beta - \phi_\beta \nabla\phi_\alpha$ is the generalized gradient vector. In the case of isotropic systems, anisotropy function $a_{\alpha\beta}(\vec{q}_{\alpha\beta})$ is equal to 1. The generalized obstacle type potential energy term is derived as

$$\omega(\boldsymbol{\phi}) = \begin{cases} \dfrac{16}{\pi^2} \displaystyle\sum_{\substack{\alpha,\beta=1 \\ (\alpha<\beta)}}^{N,N} \gamma_{\alpha\beta}\phi_\alpha\phi_\beta + \sum_{\substack{\alpha,\beta,\delta=1 \\ (\alpha<\beta<\delta)}}^{N,N,N} \gamma_{\alpha\beta\delta}\phi_\alpha\phi_\beta\phi_\delta & , \boldsymbol{\phi} \in \Delta^{N-1} \\ \infty & , \boldsymbol{\phi} \notin \Delta^{N-1} \end{cases} . \tag{4}$$

The higher order term $\gamma_{\alpha\beta\delta}$ in (4) suppresses spurious contributions of third phases in the binary interfaces as discussed in detail in [40, 41].

To describe the driving force for the phase transformations, the differences in the grand potentials of the phases are used. These are derived from experimentally determined Gibbs energies which are stored in thermodynamic databases (i.e. CALPHAD). For an efficient calculation of the driving forces, the Gibbs energies are formulated as approximated parabolic functions of the form

$$g_\alpha(\boldsymbol{c}, T) = \sum_{i=1}^{K-1} \sum_{\substack{j=1 \\ i\leq j}}^{K-1} A_{ij}^\alpha(T)\, c_i c_j + \sum_{i=1}^{K-1} B_i^\alpha(T)\, c_i + C^\alpha(T) \tag{5}$$

with the temperature dependent fitting constants A_{ij}^α, B_i^α and C^α for each phase

α and for the components i and j.

Based on Gibbs energies g_α of the N phases, the K concentrations $\boldsymbol{c}$ and the $N \times K$ chemical potentials $\boldsymbol{\mu}$ can be determined. Following [42], all phases in equilibrium have the same chemical potential and hence the number of $N \times K$ chemical potentials can be reduced to K. From this, subsequently the driving forces for phase transitions can be calculated as

$$\psi(\boldsymbol{\phi}, \boldsymbol{\mu}, T) = \sum_{\alpha=1}^{N} \left(g_\alpha \left(\boldsymbol{c}^\alpha(\boldsymbol{\mu}, T), T \right) - \sum_{i=1}^{K} \mu_i c_i^\alpha(\boldsymbol{\mu}, T) \right) h_\alpha(\boldsymbol{\phi}) \,. \tag{6}$$

To interpolate the driving forces, the function

$$h_\alpha(\boldsymbol{\phi}) = \phi_\alpha^2 \left(\sum_{\beta=1}^{N} \phi_\beta^2 \right)^{-1} \tag{7}$$

from [43] is used.

The evolution equations for the N order parameters are derived from the grand potential functional (1) by using the Allen-Cahn approach as

$$\tau \epsilon \frac{\partial \phi_\alpha}{\partial t} = - \underbrace{\frac{\partial \Upsilon(\boldsymbol{\phi}, \nabla \boldsymbol{\phi})}{\partial \phi_\alpha} + \nabla \cdot \frac{\partial \Upsilon(\boldsymbol{\phi}, \nabla \boldsymbol{\phi})}{\partial \nabla \phi_\alpha} - \frac{\partial \psi(\boldsymbol{\phi}, \boldsymbol{\mu}, T)}{\partial \phi_\alpha}}_{\frac{\delta \Psi}{\delta \phi_\alpha}} + \lambda \,. \tag{8}$$

The kinetic coefficient τ is defined as

$$\tau = \sum_{\substack{\alpha,\beta=1 \\ (\alpha<\beta)}}^{N,N} \tau_{\alpha\beta} \phi_\alpha \phi_\beta \left(\sum_{\substack{\alpha,\beta=1 \\ (\alpha<\beta)}}^{N,N} \phi_\alpha \phi_\beta \right)^{-1} \tag{9}$$

with the reciprocal mobility $\tau_{\alpha\beta}$ of the interface between the phases α and β. The Lagrange multiplier $\lambda = \frac{1}{N} \sum_{\alpha=1}^{N} {}^{\delta\Psi}/_{\delta\phi_\alpha}$ is introduced following [41] to ensure the constraint $\sum_{\alpha=1}^{N} {}^{\partial\phi_\alpha}/_{\partial t} = 0$.

2.2. Derivation of the chemical potential equation

The mass conservation and the different diffusion paths are described by a concentration model based on Fick's Laws:

$$\begin{aligned} \frac{\partial \boldsymbol{c}}{\partial t} &= \left(\frac{\partial \boldsymbol{c}}{\partial \boldsymbol{\mu}} \right)_{T,\boldsymbol{\phi}} \frac{\partial \boldsymbol{\mu}}{\partial t} + \left(\frac{\partial \boldsymbol{c}}{\partial \boldsymbol{\phi}} \right)_{T,\boldsymbol{\mu}} \frac{\partial \boldsymbol{\phi}}{\partial t} + \left(\frac{\partial \boldsymbol{c}}{\partial T} \right)_{\boldsymbol{\mu},\boldsymbol{\phi}} \frac{\partial T}{\partial t} \\ &= \nabla \cdot \left(\boldsymbol{M}(\boldsymbol{\phi}, T) \nabla \boldsymbol{\mu} \right) . \end{aligned} \tag{10}$$

Following [34–36], the evolution of the chemical potentials is used to efficiently calculate the coupled evolution of concentrations and phase-fields. By

reordering eq. (10) the evolution equations for the K chemical potentials can be written as:

$$\begin{aligned}\frac{\partial \boldsymbol{\mu}}{\partial t} = &\left[\sum_{\alpha=1}^{N} h_\alpha(\boldsymbol{\phi}) \left(\frac{\partial \boldsymbol{c}^\alpha(\boldsymbol{\mu}, T)}{\partial \boldsymbol{\mu}}\right)\right]^{-1} \\ &\Bigg(\nabla \cdot \Big(\boldsymbol{M}(\boldsymbol{\phi}, \boldsymbol{\mu}, T) \nabla \boldsymbol{\mu}\Big) \\ &- \sum_{\alpha=1}^{N} \boldsymbol{c}^\alpha(\boldsymbol{\mu}, T) \frac{\partial h_\alpha(\boldsymbol{\phi})}{\partial t} \\ &- \sum_{\alpha=1}^{N} h_\alpha(\boldsymbol{\phi}) \left(\frac{\partial \boldsymbol{c}^\alpha(\boldsymbol{\mu}, T)}{\partial T}\right) \frac{\partial T}{\partial t}\Bigg). \end{aligned} \tag{11}$$

The concentrations and the derivatives for $\partial \boldsymbol{c}^\alpha(\boldsymbol{\mu},T)/\partial \boldsymbol{\mu}$ as well as $\partial \boldsymbol{c}^\alpha(\boldsymbol{\mu},T)/\partial T$ are derived from the approximated parabolic Gibbs energies. In isothermal systems the last term is zero. The mobility function $\boldsymbol{M}(\boldsymbol{\phi}, \boldsymbol{\mu}, T)$ describing the diffusion mechanisms is modeled similar to [25] and [23].

For solid state sintering, the diffusion mechanisms can be divided into volume, grain boundary and surface diffusion [3]. The different diffusion paths are exemplary depicted in Fig. 2 b) for an idealized two particle setting. The plot in Fig. 2 a) shows the diffusion coefficient as well as the phase-field values of the grains along a cut through both particles.

A tensor of third order $\boldsymbol{\mathcal{D}} = \mathcal{D}_{i,\alpha,\beta}$ with the dimension $K \times N \times N$ is used in this work to describe the different diffusion mechanisms. This diffusion tensor $\boldsymbol{\mathcal{D}}$ can be divided into three parts

$$\boldsymbol{\mathcal{D}} = \boldsymbol{\mathcal{D}}^{vol} + \boldsymbol{\mathcal{D}}^{gb} + \boldsymbol{\mathcal{D}}^{surf}, \tag{12}$$

with the volume diffusion $\boldsymbol{\mathcal{D}}^{vol}$, the grain boundary diffusion $\boldsymbol{\mathcal{D}}^{gb}$ and the surface diffusion $\boldsymbol{\mathcal{D}}^{surf}$ being defined by

$$\boldsymbol{\mathcal{D}}^{\mathrm{vol}} := \mathcal{D}_{i,\alpha,\beta=\alpha} \tag{13}$$

$$\boldsymbol{\mathcal{D}}^{\mathrm{gb}} := \mathcal{D}_{i,\alpha\neq\mathsf{vap},\beta\neq\alpha} \tag{14}$$

$$\boldsymbol{\mathcal{D}}^{\mathrm{surf}} := \mathcal{D}_{i,\alpha\neq\beta,\beta=\mathsf{vap}} \tag{15}$$

with vap as the label for the atmospheric phase surrounding the particles in the green body. All other elements in the third order tensors $\boldsymbol{\mathcal{D}}^{vol}$, $\boldsymbol{\mathcal{D}}^{gb}$ and $\boldsymbol{\mathcal{D}}^{surf}$ are zero. For each component a symmetric diffusion matrix of the form

$$\boldsymbol{\mathcal{D}}_i = \begin{bmatrix} \mathcal{D}_{i,1,1} & \mathcal{D}_{i,2,1} & \dots & \mathcal{D}_{i,N-1,1} & \mathcal{D}_{i,N,1} \\ & \mathcal{D}_{i,2,2} & \ddots & \vdots & \vdots \\ & & \ddots & \mathcal{D}_{i,N-1,N-2} & \\ & & & \mathcal{D}_{i,N-1,N-1} & \mathcal{D}_{i,N,N-1} \\ & & & & \mathcal{D}_{i,N,N} \end{bmatrix} \tag{16}$$

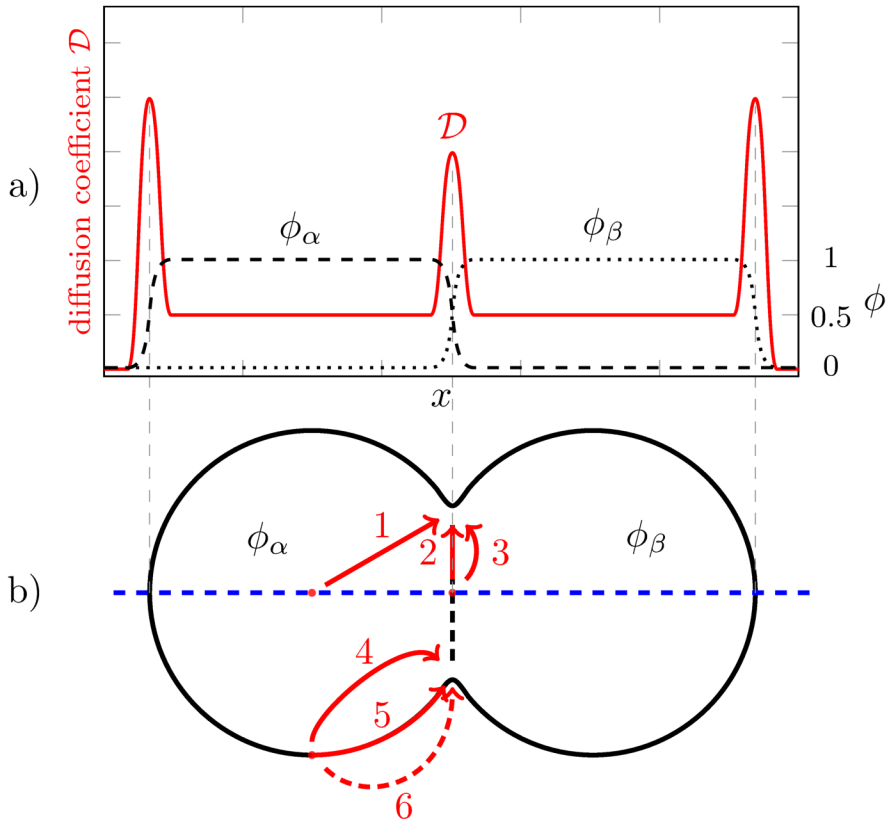

Figure 2: Relationship between the diffusion paths and the diffusion coefficient in a two particle system. a) The diffusion constant over the domain and the phase-field profile. b) The different diffusion paths, where the lines 1,3 and 4 represent the volume diffusion, 5 the surface diffusion, 2 the grain boundary diffusion and 6 evaporation and condensation.

can be written. Depending on the combination of α, β and vap, the grain boundary diffusion $\boldsymbol{\mathcal{D}}^{\mathrm{gb}}$ or the surface diffusion $\boldsymbol{\mathcal{D}}^{\mathrm{surf}}$ is described. With this the component dependent vector valued mobility function $\boldsymbol{M}(\boldsymbol{\phi}, \boldsymbol{\mu}, T)$ from eq. (11) can be noted as

$$\begin{aligned}\boldsymbol{M}(\boldsymbol{\phi},\boldsymbol{\mu},T) = &\sum_{\alpha=1}^{N} && \left(\boldsymbol{\mathcal{D}}^{\mathrm{vol}}\right)_{\alpha,\alpha} && \left(\frac{\partial \boldsymbol{c}^{\alpha}(\boldsymbol{\mu},T)}{\partial \boldsymbol{\mu}} h^{*}_{\alpha}(\boldsymbol{\phi})\right) \\ &+ \sum_{\alpha=1}^{N-1} && \left(\boldsymbol{\mathcal{D}}^{\mathsf{surf}}\right)_{\alpha,\mathsf{vap}} && \left(\frac{\partial \boldsymbol{c}^{\alpha}(\boldsymbol{\mu},T)}{\partial \boldsymbol{\mu}} h^{*}_{\alpha}(\boldsymbol{\phi}) + \frac{\partial \boldsymbol{c}^{\mathsf{vap}}(\boldsymbol{\mu},T)}{\partial \boldsymbol{\mu}} h^{*}_{\mathsf{vap}}(\boldsymbol{\phi})\right) \phi_\alpha \phi_{\mathsf{vap}} \\ &+ \sum_{\alpha=1}^{N-1} \sum_{\substack{\beta=1 \\ \alpha<\beta}}^{N-1} && \left(\boldsymbol{\mathcal{D}}^{\mathsf{gb}}\right)_{\alpha,\beta} && \left(\frac{\partial \boldsymbol{c}^{\alpha}(\boldsymbol{\mu},T)}{\partial \boldsymbol{\mu}} h^{*}_{\alpha}(\boldsymbol{\phi}) + \frac{\partial \boldsymbol{c}^{\beta}(\boldsymbol{\mu},T)}{\partial \boldsymbol{\mu}} h^{*}_{\beta}(\boldsymbol{\phi})\right) \phi_\alpha \phi_\beta \end{aligned} \tag{17}$$

where the inverse curvature of the Gibbs free energies is interpolated linearly with the phase-field in the case of boundary diffusion. The interpolation function is given by $h^*_\alpha(\boldsymbol{\phi}) = \phi_\alpha$.

3. Implementation and Optimization

The model is implemented in the massive parallel PACE3D framework ("Parallel Algorithms for Crystal Evolution in 3D") [38]. The evolution equations (8) and (11) are discretized in space with a finite difference scheme and in time with an explicit Euler method similar to [39, 40]. The discretized functions are implemented as sweeps [44] and explicitly vectorized using AVX2 intrinsics. The sweeps are optimized using node level performance engineering techniques, buffering techniques [39] and performance measuring tools like the Intel architecture code analyzer (IACA) [45], the lightweight performance-oriented tool suite for x86 multicore environments (LIKWID) [46] and the Roofline model [47, 48] to efficiently exploit current HPC hardware.

To reduce the memory requirements for the calculation of an arbitrary number of phases, the concept of Kim et al. [49] with a local reduction of the order-parameter is used. Additionally, a class based concept for the material parameters is introduced. All phases with the same material parameters are collected in one class. With this the parameter matrices which depend on the size of the phase-field vector N can be reduced for the considered system Al-O to the two classes Al_2O_3 and O_2. With this, e.g. the interface energy matrix is reduced from $N \times N$ entries to 2×2 entries.

The voxel data is read and written in PACE3D with MPI-IO. Additionally, to reduce the simulation data the iso-surface of the grain structure is efficiently written as mesh data using multiple master processes [38].

4. Material Parameters

For the simulations of the sintering process, the material system Al-O with its solid phase γ-Al_2O_3 is used as there is a multitude of experimental data available [50–53]. The powder compacts were assumed to sinter in an oxygen atmosphere. The interface energies between solid and gas are derived from [50]. The ratio of the solid-solid interfacial energy to the solid-gas interfacial energy was assumed to be 5/6. The diffusion coefficient D_v for the volume diffusion in Al_2O_3 is obtained from [52]. The diffusion coefficients in the grain boundary and surface are set to $D_{gb} = 1000 \cdot D_v$ and $D_{surf} = 1000 \cdot D_v$. In order to avoid timescale problems and to reduce the computational effort, the diffusion coefficient in the gas is chosen to $D_{gas} = 0.5 \cdot D_v$, similar to [54]. The kinetic coefficient τ is derived based on [35]. The dimensionless simulation parameters and their physical values are summarized in Table 1.

In order to simulate the system Al-O, the Gibbs energies are modeled based on the CALPHAD-database from Hashimoto and co-workers [55]. The database is published by the National Institute for Material Science (NIMS) of Japan and

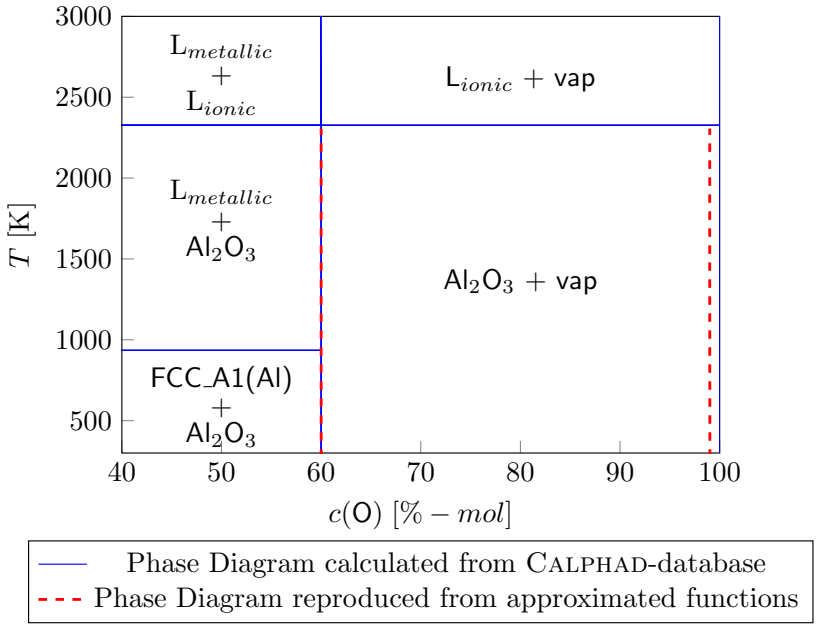

Figure 3: Phase diagram of Al-O generated from CALPHAD-database [53, 55] (blue solid lines) and recalculated phase diagram from approximated parabolic Gibbs energy functions of the phases Al_2O_3 and vap (red dashed lines).

bases on experimental data from Lee and Saunders [53]. From this database, approximated parabolic functions at the operating temperature are derived for each phase class as described in [56, 57] to reduce the computational effort. For the binary system Al-O, the general approach of equation (5) can be reduced to

$$g_\alpha(c_O, T) = A^\alpha(T)\, c_O^2 + B^\alpha(T) c_O + C^\alpha(T) \tag{18}$$

with c_O as the concentration of oxygen. To reproduce the stoichiometric character of the grain phases Al_2O_3 and the vapour phase vap the equilibrium concentrations are set to temperature-independent values. Further the fitted coefficients $B^\alpha(T)$ and $C^\alpha(T)$ are modelled with a quadratic temperature dependence. The adjustable parameter A^α is chosen to ensure that the phases Al_2O_3 and vap can be reproduced with their correct stoichiometric composition for a wide temperature range as shown in Fig. 3 for the considered part of the phase diagram of Al-O. Thus the approximated Gibbs energy functions can be written as

$$g_\alpha(c_O, T) = A^\alpha\, c_O^2 + (B_3^\alpha T^2 + B_2^\alpha T + B_1^\alpha) c_O + C_3^\alpha T^2 + C_2^\alpha T + C_1^\alpha\,. \tag{19}$$

Table 1: Summary of the dimensionless simulation parameters and their values in physical units for Al-O.

parameter	simulation value	physical value	source
Numerical parameters			
Δx	1	50 nm	-
Δt	0.0211	52.75 µs	volume diffusion
	0.0125	31.25 µs	boundary diffusion
ϵ	$3 \cdot \Delta x$	150 nm	-
$\gamma_{\alpha\beta\delta}$	80		derived based on [40]
Physical parameters			
$\boldsymbol{\mathcal{D}}^{vol}_{grain}$	0.01	$1 \times 10^{-14}\,\mathrm{m^2/s}$	[52]
$\boldsymbol{\mathcal{D}}^{vol}_{\mathsf{vap}}$	0.005	$0.5 \times 10^{-14}\,\mathrm{m^2/s}$	-
$\boldsymbol{\mathcal{D}}^{gb}$	10	$1 \times 10^{-11}\,\mathrm{m^2/s}$	-
$\boldsymbol{\mathcal{D}}^{surf}$	10	$1 \times 10^{-11}\,\mathrm{m^2/s}$	-
T	1	1708.15 K	-
$\boldsymbol{c}_{\mathsf{Al_2O_3}}\,[c_{\mathsf{O}}, c_{\mathsf{Al}}]$	0.6, 0.4	60, 40 mol-%	[53, 55]
$\boldsymbol{c}_{\mathsf{vap}}\,[c_{\mathsf{O}}, c_{\mathsf{Al}}]$	0.99, 0.01	99, 1 mol-%	[53, 55]
$\gamma_{\mathsf{grains,vap}}$	4	$0.8\,\mathrm{J/m^2}$	γ-$\mathsf{Al_2O_3}$ from [50]
$\boldsymbol{\gamma}$	phase classes: grains, vap	$\begin{bmatrix} 5/6 & 1 \\ 1 & - \end{bmatrix} \cdot \gamma_{\mathsf{grains,vap}}$	-
Gibbs energy parameters of eq. (18) *at temperature* T = 1708.15 K			
A^{vap}	10	$1000\,\mathrm{kJ/mol}$	chosen for stoichiometry
B^{vap}	−20.95	$-2095\,\mathrm{kJ/mol}$	calculated from [53, 55]
C^{vap}	6.632	$663.2\,\mathrm{kJ/mol}$	calculated from [53, 55]
A^{grains}	50	$5000\,\mathrm{kJ/mol}$	chosen for stoichiometry
B^{grains}	−61.16	$-6115\,\mathrm{kJ/mol}$	calculated from [53, 55]
C^{grains}	14.83	$1483\,\mathrm{kJ/mol}$	calculated from [53, 55]

5. Results

In the following section the model is qualitatively and quantitatively validated by using a two particle setting in 2D and 3D based on [3, 23, 58]. Subsequently, 3D simulations of realistic green-bodies with different active diffusion mechanisms are investigated.

5.1. Simulation of the two particle case

In the initial sintering stage, necks form between the particles [59]. Depending on the dominant diffusion mechanism the rate at which these necks grow changes. To validate the derived phase-field model, the neck radius evolution from the simulations is compared to analytical equations.

The simulation setting for the two particle system is schematically shown in Fig. 2. As boundary conditions, for both evolution equations, no flux conditions are used. The particle radius was chosen to be 2.5 µm = 50 cells. As initial conditions the equilibrium concentrations of the respective phases are used. The material parameters used for the simulations are given in Table 1. Systematic studies with (de)activated volume diffusion D_v, grain boundary diffusion D_{gb} and surface diffusion D_s are conducted. Therefore, the two-particle simulations TP_v, TP_{v+gb}, TP_{v+s} and TP_{v+gb+s}, labelled by the activated diffusion mechanisms, are considered.

Fig. 4 shows the evolution for different sets of active diffusion mechanisms. The contour lines of the grain-gas interface are depicted at four different time steps.

@All: [W: the weird thing here is that GB diffusion (or volume diffusion in the vicinity of the GB) is NEEDED to get densification, while surface diffusion only will result in coarsening, but not in densification. What you in principle do in here is that you add faster diffusion as you add additional diffusion mechanisms. Since the phase field model is a diffuse interface model, there is no such thing as pure GB or surface diffusoin or as pure volume diffusion. All you can do is enhancing the diffusion at a specific location. Having said that it is somewhat unexpected that, for GB+V, the evolution is allmost the same as only for V and no densification occurs, while for whenever S is involved, quite some densification occured. This needs to be commented somehow in the manuscript. Could it be that this is just because of the high relative GB energy (relative to the surface energy), so that the driving force situation is the problem? [M+J: Hierüber sollten wir nochmal über die anmerkung auf Seite 15 reden weil wir das etwas anders sehen]

As expected, the neck evolutions are influenced by the dominant diffusion mechanism. The simulations with activated surface diffusion evolve faster than the others. Due to the dominance of the surface diffusion a similar evolution is observed in the simulations TP_{v+s} and TP_{v+gb+s}. As a result of the slower neck evolution compared to the simulations with surface diffusion, the contour

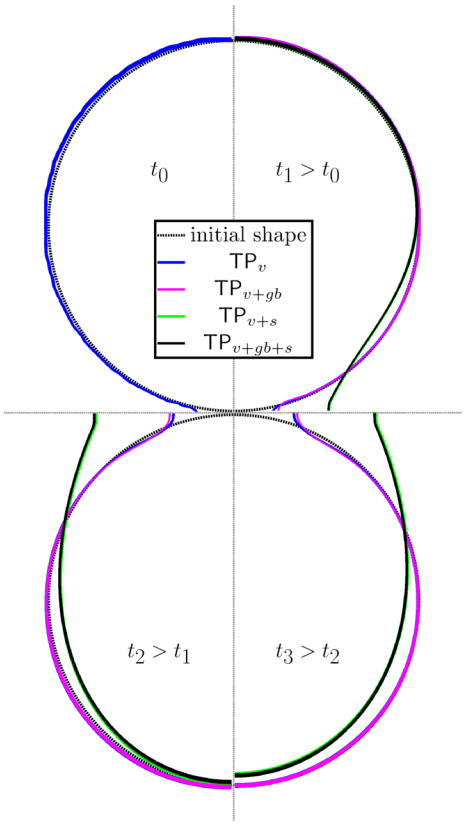

Figure 4: Contour lines of the grain-gas interface for four different parameter sets of diffusion coefficients. In each quadrant the same physical time for the four simulations is shown.

lines in the simulations TP_v and TP_{v+gb} are still close together. However, the evolution of TP_{v+gb} is faster than the evolution of TP_v.

For all cases, densification is observed since volume diffusion in the vicinity of the grain boundary occurs. In the case of active grain boundary diffusion, the enhanced diffusion coefficient is constricted to the grain boundary. Due to the lower gradients of the concentration along the grain boundary in contrast to the surface, the driving forces for the mass transport are multiple orders of magnitude smaller. Only close to the triple point there are similar driving forces for mass flux as on the surface. Hence the densification for TP_{v+gb} is similar to TP_v and smaller than in the simulations with active surface diffusion.

To highlight this combination of local driving force and the enhanced diffusion coefficient, the mass flux for the four settings is shown for exemplary states in Fig. 5. Note that the scales and shown simulation times are different in each depicted simulation in order to highlight the dominant fluxes. Hence, only in TP_v and TP_{v+gb} the flux in the bulk is visible due to the overall lower magnitude of the fluxes. For all simulations the neck region is the global sink for diffusion, although different pathways depending on the dominant diffusion mechanism are used. Due to the chosen value for bulk gas diffusion, evaporation and condensation occur as visible in Fig. 5, however, their contribution is minor. In the simulations with activated surface diffusion, the evolution is dominated by the fluxes along the surface. The effect of grain boundary diffusion is most evident for TP_{v+gb}, whereas in the other simulations the evolution is dominated by surface diffusion or volume diffusion. Both investigations, i.e. on the particle shape evolution and the fluxes, show the expected qualitative behavior for the different simulations.

Following Wang [23], the relative neck radius x/r over time t for two adjacent spheres can be quantitatively described by the power law

$$x(t)/r = A(\gamma, r) \cdot t^n \,. \tag{20}$$

The pre-exponential factor A depends on the surface energy γ and the radius r of the sphere whereas the exponent n depends on the dominant diffusion path. Based on the analysis in [3, 23] the expected exponents for volume, grain boundary and surface diffusion are $1/5 = 0.2$, $1/6 \sim 0.17$ and $1/7 \sim 0.14$, respectively. A quantitative analysis of the neck growth kinetics using equation (20) is summarized in Fig. 6. In all diagrams the relative neck radius is plotted logarithmically over time.

For constant particle sizes, the impact of the different diffusion mechanisms in two-dimensional simulations is shown in Fig. 6(a). The neck growth slope (i.e. the exponent in eq. (20)) is in accordance with the theoretical predictions. Similar agreement between theoretical predictions and simulation results is found for the three-dimensional simulations as depicted in Fig. 6(b).

Furthermore, the influence of the particle size on the sintering behavior is investigated for the setting TP_{v+s}. For different particle sizes r_i, Herring's scaling law for surface diffusion controlled growth [20] predicts that the sintering

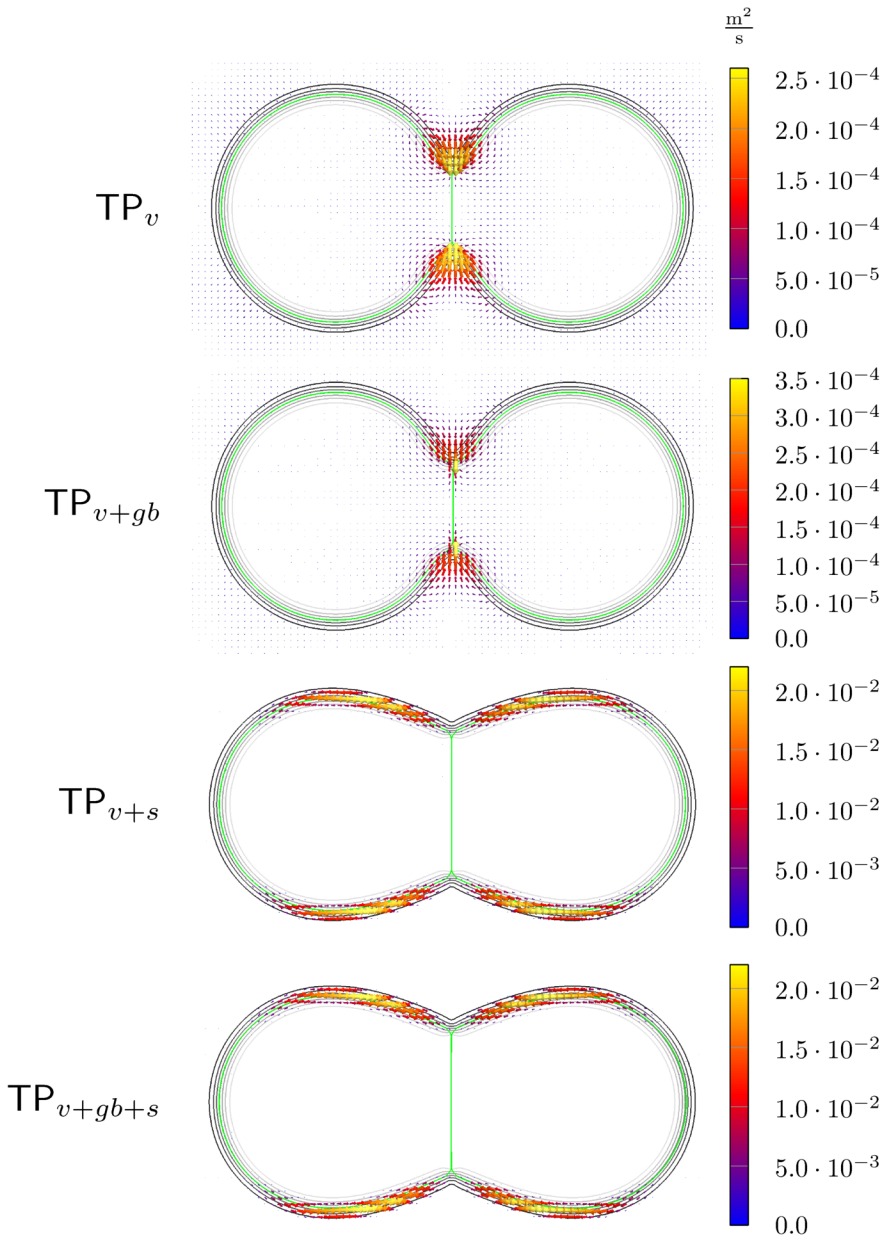

Figure 5: Mass flux during sintering for different activated diffusion mechanisms. In gray the contour lines of the diffuse interface with respect to the gas phase are shown at different iso levels. In green the iso level at $\phi_\alpha = 1/2$ of both grains is indicated. Note that the amount of flux is scaled individually as indicated by the color bars for each image and hence the fluxes can only be qualitatively compared.

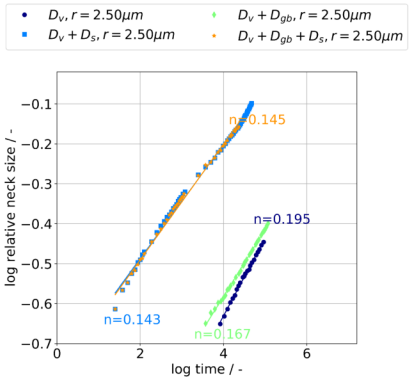

(a) variation of diffusion mechanisms

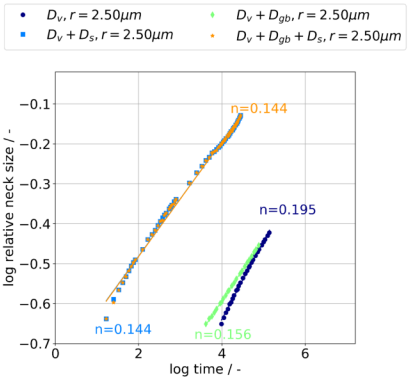

(b) variation of diffusion mechanisms, 3D

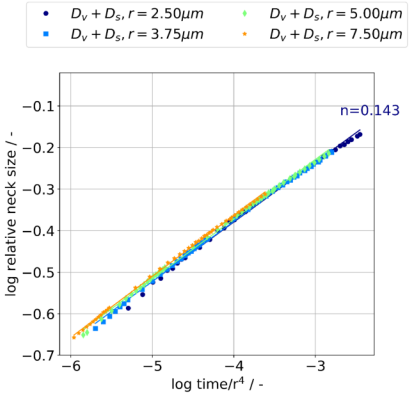

(c) Herring's scaling law for surface diffusion

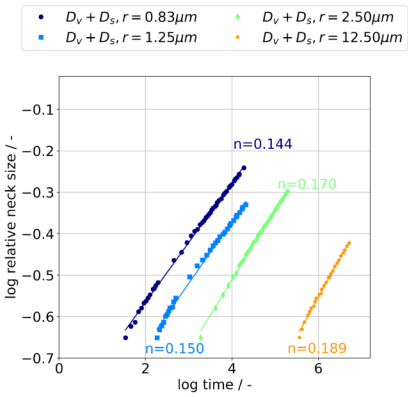

(d) transition from surface to volume diffusion (see text)

Figure 6: Evolution of neck size with different particle sizes and activated diffusion mechanisms.

rates scale as

$$\frac{\dot{X}_1/r_1}{\dot{X}_2/r_2} = \frac{r_1}{r_2}^{-4}. \tag{21}$$

By normalizing the time with r_i^{-4} all sintering curves collapse to a single master curve as shown in Fig. 6(c). Therefore the scaling law holds for the present simulations. Accordingly the slope in Fig. 6(c) is also the same for all particle radii. The same slope of approximately $1/7$ as well as scaling behavior is also found by Pino [60] with a level-set model and by Kumar [54] with a phase-field model using similar ratios of volume diffusivity to boundary diffusivity.

For increasing particle radii, the distances for the fluxes along the surface increase and the driving force decreases due to the lower curvature. Hence a transition from surface diffusion to volume diffusion as the dominant mechanism of sintering is expected with increasing particle size [10, 11].

@All: [CITE:COBLE [M+J: Draus ableiten läasst es sich, aber es steht nicht explizit drin]

To evaluate this transition in computationally efficient domain sizes, the surface diffusivity was reduced by a factor of 200 to $D_s = 5 \cdot D_v$ with the particle radii ranging from 0.83 µm to 12.50 µm. The results of this study for the setting TP_{v+s} are summarized in Fig. 6(d). As evident from the slopes of the curves, for a particle size of 0.83 µm the evolution is dominated by surface diffusion, whereas with increasing particle size the volume component becomes more dominant until at a size of 12.50 µm the evolution is mostly dominated by volume diffusion.

In summary, both the neck growth kinetics of the different diffusion scenarios and the dependence of the dominant diffusion mechanism on the particle size agree well with theoretical expectations. Accordingly, we can conclude that the two particle case is qualitatively and quantitatively reproduced in the presented simulations.

5.2. Simulation of the many-particle case

Based on the qualitative and quantitative accordance with theoretical models, large scale phase-field simulations of realistic green bodies with multiple thousand particles are conducted. With these simulations, the effect of varying active diffusion mechanisms on the densification is investigated. The green body with an initial density of 63.8% is generated with the physics engine nphysics [61] using spherical particles with a radius of 7 cells (0.35 µm). For all simulations a domain size of $400 \times 400 \times 400$ voxel cells with 24 897 particles is used, with the initial packing shown in Fig. 7. No flux conditions are used as boundary conditions for both evolution equations. The simulations are calculated on the Hazel Hen supercomputer [62] using 1 083 cores for 50 hours, calculating 10 million time steps.

Similar to the two particle settings, the different diffusion mechanisms are systematically (de)activated. This leads to four many-particle simulations MP_v, MP_{v+gb}, MP_{v+s} and MP_{v+gb+s} labelled by the activated diffusion mechanisms. To inhibit grain growth for easier comparison to the Coble model, the kinetic

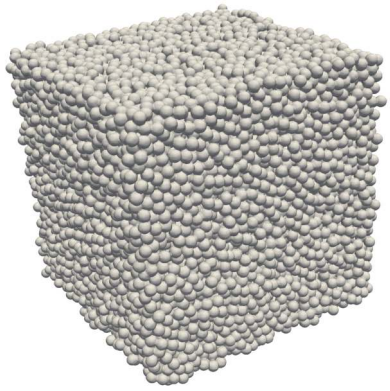

Figure 7: Initial green body with 24 897 spherical particles in a $400 \times 400 \times 400$ voxel cells domain.

coefficient τ is adjusted. Additionally, the ratio of interface energies is changed from $5/6$ to $1/3$ in order to achieve faster sintering kinetics and hence reduce the computational effort. Furthermore, these two changes of the parameters in Table 1 allow to increase the stable timestep calculated with the von Neumann stability analysis [63] for the simulation MP_v, from 52.75 µs to 877 µs. In Fig. 8 the microstructure evolutions of the four simulations at three time steps are shown. On the left, the final green bodies with the cutting planes are depicted. On the right, the corresponding two dimensional cuts illustrate the microstructural evolution. Starting from the loosely packed green body, the particles form sintering necks between each other. Later on, the green body starts to densify. With more activated diffusion mechanisms, as expected, the densification of the green bodies is faster.

To quantitatively analyze the microstructure evolution, the density over time is plotted in Fig. 9. This density is determined by applying a line-intercept analysis on the envelope of the grain phases. The analysis is done separately in each dimension and the average is calculated. For all simulations, the densification curve follows the characteristic sigmoidal shape [3]. The densification rate decreases in the sequence

$$\mathsf{MP}_{v+gb+s} > \mathsf{MP}_{v+s} > \mathsf{MP}_{v+gb} > \mathsf{MP}_{v}. \tag{22}$$

However, for the considered simulation time none of the simulations have reached full density, and open pore channels as well as isolated pores remain in the sintered body. It is expected that if the simulations were continued, complete densification would be reached.

Furthermore, in dashed lines the analytical solutions of the Coble models [3]

$$\dot{\rho}_v(t) = \frac{10 D_v \gamma V_m}{RTG^3} \tag{23}$$

$$\dot{\rho}_b(t) = \frac{{}^4\!/_3 D_b \delta_b \gamma V_m}{RTG^4 \sqrt{((1-\rho_b(t))}} \tag{24}$$

for volume diffusion ρ_v and grain boundary diffusion ρ_b are shown for constant grain size G and the used simulation parameters. Within the equation, D_v is the volume diffusion coefficient, γ is the grain-vapor interface energy, V_m is the molar volume of alumina, R is the ideal gas constant, T is the temperature, D_b is the grain boundary diffusion coefficient and δ_b is the thickness of the grain boundary diffusion layer. The analytical solutions have a similar time scale as well as a similar trend as the corresponding simulations. Initially both solutions match closely, whereas for later times, the analytical solutions predict a higher densification rate. This deviation can be explained by the geometric differences. The Coble model assumes a network of equally-sized open pore channels in which 14-faced grains of equal size are embedded. However, the initial green body is not based on the Coble geometry and also does not evolve to such a geometry. Furthermore, Coble's analysis only considers the intermediate stage of sintering, where the pore channels still form a network. As soon as the pores are isolated, a significant deviation from Coble's equations is to be expected.

@All: evtl. weiter beschreiben und entscheiden, ob Coble rein soll [w: was genau meint ihr mit Coble? Habt ihr eine entsprechende analyse gemacht? wie sieht die aus?] [M+J: extended above with figure]

The evolution of isolated pores is exemplary depicted in Fig. 10 for the simulations MP_{v+s} and MP_{v+gb+s}, to show the effect of grain boundary diffusion. The isolated pores are depicted in green. To highlight the mass flux, a representative slice is added showing the relative amount of flux as well as arrows to indicate the flux direction. Since grain boundary diffusion is inactive in Figs. 10(a) and 10(b), the majority of the mass flux occurs along the surface. However the shrinkage rate is limited due to the lack of a quick diffusion pathway as only volume diffusion can transport mass towards the pore, even though small pores with few neighbours shrink due to energy minimization. In contrast, Figs. 10(c) and 10(d) illustrate the flux being directed towards the pore for active grain boundary diffusion. Herein, the shrinkage of pores is more pronounced since the driving force has a quick diffusion pathway along the grain boundary available. Furthermore, a part of the large pore splits off due to local pinch-off.

@All: [W: ich kann das nicht im bild sehen] [M+J]: bild update]

@All: [W: vorsicht - es gibt grundsätzliche überlegungen zur stabilität von poren, welche nur von der Form abhängen und nicht von diffusionsmechanismen. Siehe im rahaman auf seite 592] [M+J: okay, aber wir wollten hier nicht weiter auf poren an sich eingehen, nur das wir welche sehen und auch verschwinden können]

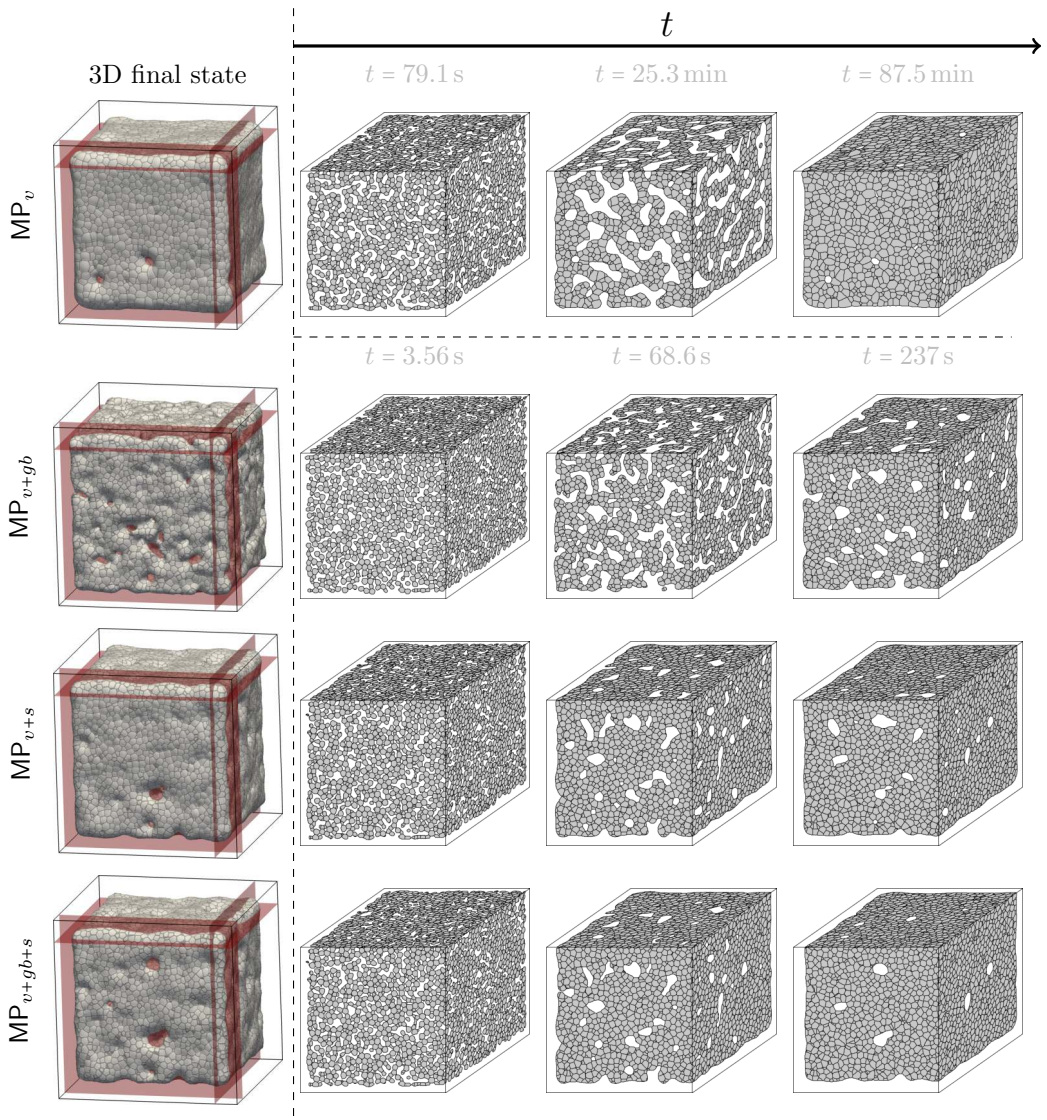

Figure 8: On the left, the final three-dimensional microstructures. In red the cutting planes for the time evolution are highlighted. On the right, the microstructural evolution over time for the different activated diffusion mechanisms is shown. Gray areas depict grains which are separated by black grain boundaries, whereas white areas depict the vapor phase. Due to the different time scales, the simulation results using only volume diffusion are shown for other physical times.

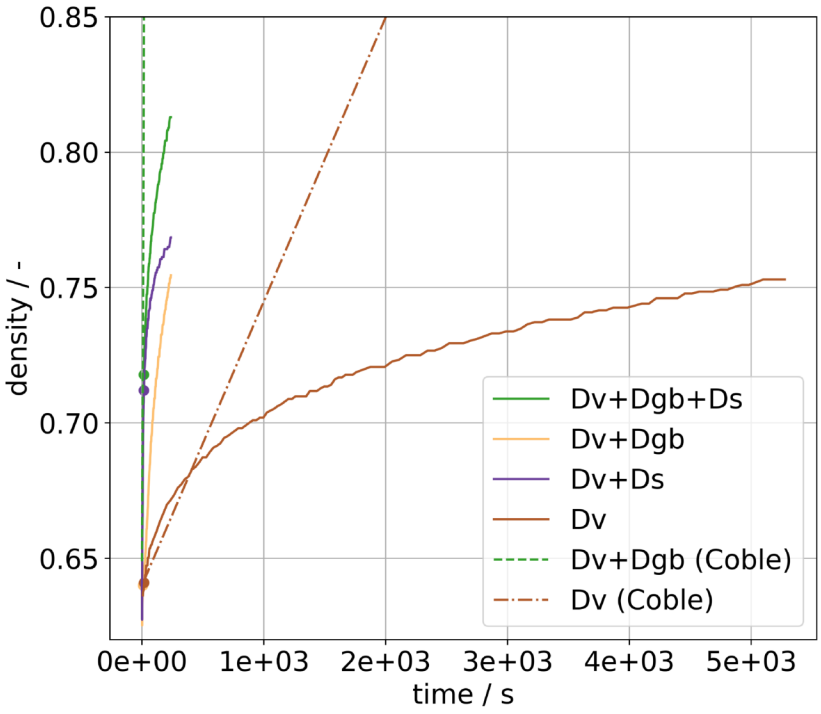

Figure 9: Evolution of density over time for the four considered simulations. The solid lines are the simulation results whereas the dash-(dotted) lines show the results of a Coble analysis.

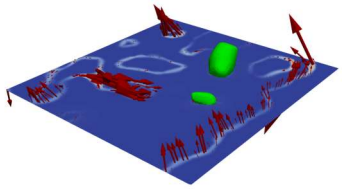

(a) Pores in MP_{v+s} at t

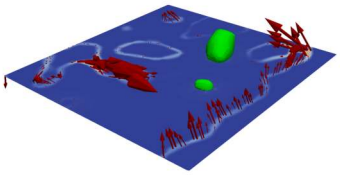

(b) Pores in MP_{v+s} at $t + n\Delta t$

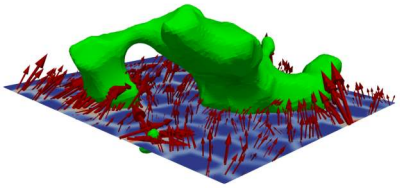

(c) Pore in MP_{v+gb+s} at $t^{'}$

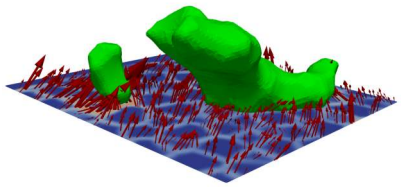

(d) Pores in MP_{v+gb+s} at $t^{'} + n\Delta t$

Figure 10: Evolution of pores (green) with and without grain boundary diffusion. Furthermore, a slice through the domain is selected to highlight the magnitude of the mass flux. The mass flux increases from blue over white to red within the slice with the arrows being scaled with the magnitude. The arrows additionally demonstrate the direction of mass flux within the slice. In the simulation MP_{v+s}, the majority of the mass flux occurs along the surface. As the surface of the isolated pore is separated from the rest of the vapor phase, there is no quick kinetic pathway for mass transport to the pore, hence the shrinkage rate is limited. In contrast, MP_{v+gb+s} shows the vanishing of a small pore as well as a larger pore splitting due to the mass flux being directed towards the pores along the grain boundaries.

6. Conclusion

In this work, a novel model for sintering using the grand potential approach combined with different diffusion pathways has been developed and implemented efficiently in the multi-physics Pace3D framework. Using this model, the results of two-particle setting simulations are compared with the theoretical predictions in two and three dimensions. Afterwards large-scale phase-field simulations of a realistic green body are conducted.

In these simulations the densification rate decreases in the following order: $\mathsf{MP}_{v+gb+s} > \mathsf{MP}_{v+s} > \mathsf{MP}_{v+gb} > \mathsf{MP}_{v}$. Furthermore the appearance of isolated pores was observed in the large-scale simulations. The lifetime of the isolated pores is mainly dependent on whether grain boundary diffusion is active or not. From the results, we draw the following conclusions:

(i) The neck radius evolution in the two particle setting is in quantitative accordance with the theory for different active diffusion mechanisms in 2D and 3D.

(ii) Furthermore Herring's scaling law for surface diffusion applies in the two particle setting.

(iii) The present model contains the transition from a surface diffusion dominated process to a volume diffusion dominated process.

(iv) The region of major mass flux changes, depending on the dominant diffusion mechanism.

(v) Isolated pores appear in large-scale simulations which indicates that they freely evolved during the sintering process without being present in the model or in the initial setup.

(vi) Due to the observed correlation between grain boundary diffusion and pore stability, it can be concluded that the presented model can be used to investigate the evolution of pores in a qualitative manner.

Based upon these observations and conclusions, the presented model is capable for the usage in further investigations. In future works, the effects of initial conditions as well as material and process parameters on the densification, grain growth and pore evolution during the sintering process are of special interest.

7. Acknowledgment

We are grateful to the computational resources on the Hazel Hen provided by the HLRS Stuttgart and on the ForHLR II at the KIT. Further the authors thank for the financial support within the project SKAMPY (Ultra-scalable multiphysics simulations for solidification processes in metals) funded by BMBF and the cooperative graduate school "Gefügeanalyse und Prozessbewertung" by the ministry of Baden-Wuerttemberg.

References

[1] R. K. Bordia, S.-J. L. Kang, E. A. Olevsky, Current understanding and future research directions at the onset of the next century of sintering science and technology, Journal of the American Ceramic Society (2017).

[2] J. Hötzer, M. Kellner, P. Steinmetz, B. Nestler, Applications of the Phase-Field Method for the Solidification of Microstructures in Multi-Component Systems, Journal of the Indian Institute of Science 96 (2016) 235–256.

[3] M. N. Rahaman, Ceramic Processing and Sintering (Materials Engineering) 1 (2003).

[4] S.-J. L. Kang, Sintering: densification, grain growth and microstructure, Butterworth-Heinemann, 2004.

[5] K. Deniz, Herstellung und Eigenschaften von Optokeramiken auf der Basis von Mg-Spinell und Aluminiumoxid, Karlsruhe Institute of Technology, 2011.

[6] J. Svoboda, H. Riedel, New solutions describing the formation of interparticle necks in solid-state sintering, Acta Metallurgica et Materialia 43 (1995) 1–10.

[7] J. Frenkel, Viscous flow of crystalline bodies under the action of surface tension, J. Phys. (U. S. S. R) 9 (1945) 385.

[8] G. C. Kuczynski, Self-diffusion in Sintering of Metallic Particles, Trans. Metall. Soc. AIME (1949) 169–178.

[9] W. D. Kingery, M. Berg, Study of the Initial Stages of Sintering by Viscous Flow, Evaporation—Condensation, and Self-Diffusion, Journal of Applied Physics 26 (1955).

[10] R. L. Coble, Sintering crystalline solids. i. intermediate and final state diffusion models, Journal of applied physics 32 (1961) 787–792.

[11] R. L. Coble, Sintering crystalline solids. ii. experimental test of diffusion models in powder compacts, Journal of applied physics 32 (1961) 793–799.

[12] J. E. Burke, D. Turnbull, Recrystallization and grain growth, Progress in Metal Physics 3 (1952) 220–292.

[13] M. Hillert, On the theory of normal and abnormal grain growth, Acta Metall. Mater. 13 (1965) 227–238.

[14] R. J. Brook, Pore-Grain Boundary Interactions and Grain Growth, J. Am. Ceram. Soc. 52 (1969) 56–57.

[15] F. Nichols, Kinetics of diffusional motion of pores in solids, J Nucl Mater 30 (1969) 143–165.

[16] F. M. A. Carpay, Discontinuous grain growth and pore drag, J. Am. Ceram. Soc. 60 (1977) 2–3.

[17] M. Spears, A. Evans, microstructure development during final/intermediate stage sintering -II. Grain and pore coarsening 30 (1982) 1281–1289.

[18] H. Riedel, J. Svoboda, A theoretical study of grain growth in porous solids during sintering, Acta Metall. Mater. 41 (1993) 1929–1936.

[19] R. M. German, The emergence of quantitative sintering theory from 1945 to 1955, JOM 69 (2017) 630–634.

[20] C. Herring, Effect of change of scale on sintering phenomena, Journal of Applied Physics 21 (1950) 301–303.

[21] A. Kazaryan, Y. Wang, B. R. Patton, Generalized phase field approach for computer simulation of sintering: incorporation of rigid-body motion, Scripta materialia 41 (1999) 487–492.

[22] X. Jing, J. Zhao, L. He, 2D aggregate evolution in sintering due to multiple diffusion approaches, Materials chemistry and physics 80 (2003) 595–598.

[23] Y. U. Wang, Computer modeling and simulation of solid-state sintering: A phase field approach, Acta Materialia 54 (2006) 953–961.

[24] K. Asp, J. Ågren, Phase-field simulation of sintering and related phenomena–a vacancy diffusion approach, Acta materialia 54 (2006) 1241–1248.

[25] V. Kumar, Z. Fang, P. Fife, Phase field simulations of grain growth during sintering of two unequal-sized particles, Materials Science and Engineering: A 528 (2010) 254–259.

[26] K. Chockalingam, V. Kouznetsova, O. van der Sluis, M. Geers, 2D Phase field modeling of sintering of silver nanoparticles, Computer Methods in Applied Mechanics and Engineering (2016).

[27] J. Deng, A phase field model of sintering with direction-dependent diffusion, Materials Transactions 53 (2012) 385–389.

[28] K. Shinagawa, Simulation of grain growth and sintering process by combined phase-field/discrete-element method, Acta Materialia 66 (2014) 360–369.

[29] S. Biswas, D. Schwen, J. Singh, V. Tomar, A study of the evolution of microstructure and consolidation kinetics during sintering using a phase field modeling based approach, Extreme Mechanics Letters 7 (2016) 78–89.

[30] S. Biswas, D. Schwen, V. Tomar, Implementation of a phase field model for simulating evolution of two powder particles representing microstructural changes during sintering, Journal of Materials Science (2017) 1–27.

[31] R.-J. Zhang, Z.-W. Chen, F. Wei, X.-H. Qu, Thermodynamic consistent phase field model for sintering process with multiphase powders, Transactions of Nonferrous Metals Society of China 24 (2014) 783–789.

[32] Y. Wang, Y. Liu, C. Ciobanu, B. R. Patton, Simulating microstructural evolution and electrical transport in ceramic gas sensors, Journal of the American Ceramic Society 83 (2000) 2219–2226.

[33] R. Mukherjee, T. Chakrabarti, E. A. Anumol, T. A. Abinandanan, N. Ravishankar, Thermal stability of spherical nanoporous aggregates and formation of hollow structures by sintering– a phase-field study, ACS nano 5 (2011) 2700–2706.

[34] M. Plapp, Unified derivation of phase-field models for alloy solidification from a grand-potential functional, Physical Review E 84 (2011) 031601.

[35] A. Choudhury, B. Nestler, Grand-potential formulation for multicomponent phase transformations combined with thin-interface asymptotics of the double-obstacle potential, Physical Review E 85 (2012) 021602.

[36] J. Hötzer, M. Jainta, P. Steinmetz, B. Nestler, A. Dennstedt, A. Genau, M. Bauer, H. Köstler, U. Rüde, Large scale phase-field simulations of directional ternary eutectic solidification, Acta Materialia 93 (2015) 194 – 204.

[37] S. G. Kim, W. T. Kim, T. Suzuki, M. Ode, Phase-field modeling of eutectic solidification, Journal of crystal growth 261 (2004) 135–158.

[38] J. Hötzer, A. Reiter, H. Hierl, P. Steinmetz, M. Selzer, B. Nestler, The parallel multi-physics phase-field framework pace3d, Journal of Computational Science 26 (2018) 1 – 12.

[39] J. Hötzer, Massiv-parallele und großskalige Phasenfeldsimulationen zur Untersuchung der Mikrostrukturentwicklung, volume 70, KIT Scientific Publishing, 2017.

[40] J. Hötzer, O. Tschukin, M. B. Said, M. Berghoff, M. Jainta, G. Barthelemy, N. Smorchkov, D. Schneider, M. Selzer, B. Nestler, Calibration of a multiphase field model with quantitative angle measurement, Journal of Materials Science 51 (2015) 1788–1797.

[41] B. Nestler, H. Garcke, B. Stinner, Multicomponent alloy solidification: phase-field modeling and simulations, Physical Review E 71 (2005) 041609.

[42] M. Kellner, I. Sprenger, P. Steinmetz, J. Hötzer, B. Nestler, M. Heilmaier, Phase-field simulation of the microstructure evolution in the eutectic NiAl-34Cr system, Computational Materials Science 128 (2017) 379–387.

[43] N. Moelans, A quantitative and thermodynamically consistent phase-field interpolation function for multi-phase systems, Acta Materialia 59 (2011) 1077–1086.

[44] S. Donath, Wetting models for a parallel high-performance free surface lattice Boltzmann method, Verlag Dr. Hut, 2011.

[45] Intel architecture code analyzer, version 2.1, `https://software.intel.com/en-us/articles/intel-architecture-code-analyzer`, 2015. [Online; accessed March-2015].

[46] J. Treibig, G. Hager, G. Wellein, LIKWID: A lightweight performance-oriented tool suite for x86 multicore environments, in: Proceedings of PSTI2010, the First International Workshop on Parallel Software Tools and Tool Infrastructures, 2010.

[47] S. Williams, A. Waterman, D. Patterson, Roofline: an insightful visual performance model for multicore architectures, Communications of the ACM 52 (2009) 65–76.

[48] J. D. McCalpin, Memory bandwidth and machine balance in current high performance computers, IEEE Computer Society Technical Committee on Computer Architecture (TCCA) Newsletter (1995) 19–25.

[49] S. G. Kim, D. I. Kim, W. T. Kim, Y. B. Park, Computer simulations of two-dimensional and three-dimensional ideal grain growth 74 (2006) 061605.

[50] J. M. McHale, Surface Energies and Thermodynamic Phase Stability in Nanocrystalline Aluminas, Science 277 (1997) 788–791.

[51] A. H. Tavakoli, P. S. Maram, S. J. Widgeon, J. Rufner, K. Van Benthem, S. Ushakov, S. Sen, A. Navrotsky, Amorphous alumina nanoparticles: Structure, surface energy, and thermodynamic phase stability, Journal of Physical Chemistry C 117 (2013) 17123–17130.

[52] R. H. Doremus, Diffusion in alumina, Journal of Applied Physics 100 (2006).

[53] B.-J. Lee, N. Saunders, Thermodynamic evaluation of the Ti-Al-O ternary system, Zeitschrift für Metallkunde 88 (1997) 152–161.

[54] V. Kumar, Simulations and Modeling of Unequal Sized Particles Sintering, Ph.D dissertation (2011) 163.

[55] K. Hashimoto, T. Abe, Y. Sawada, AlO, CALPHAD database, Particle Simulation and Thermodynamics Group, National Institute for Materials Science, 2011.

[56] K. D. Noubary, M. Kellner, P. Steinmetz, J. Hötzer, B. Nestler, Phase-field study on the effects of process and material parameters on the tilt angle during directional solidification of ternary eutectics, Computational Materials Science 138 (2017) 403–411.

[57] A. Choudhury, M. Kellner, B. Nestler, A method for coupling the phase-field model based on a grand-potential formalism to thermodynamic databases, Current Opinion in Solid State and Materials Science 19 (2015) 287–300.

[58] H. E. Exner, Grundlagen von Sintervorgängen : mit 7 Tabellen, Ph.D. thesis, Berlin, 1978.

[59] R. L. Coble, Initial sintering of alumina and hematite (1958).

[60] D. H. Pino Muñoz, High-performance computing of sintering process at particle scale, Ph.D. thesis, 2012.

[61] S. Crozet, nphysics physics engine, `http://nphysics.org/`, ???? Accessed: 02.02.2018.

[62] C. A. Müller, et al., Gauss centre for supercomputing, 2014. [Online; accessed March-2018].

[63] E. Isaacson, H. Keller, Analysis of Numerical Methods, Dover Books on Mathematics, Dover Publications, 1994.